The Pleiades Reflection Nebula. II. Simple Model Constraints on Dust Properties and Scattering Geometry

Steven J. Gibson[1], Kenneth H. Nordsieck[2]

ABSTRACT

We have used wide-field ultraviolet, optical and far-infrared photometric images of Pleiades reflection nebulosity to analyze dust properties and the 3-D nebular geometry. Scattered light data were taken from 1650 & 2200 Å *Wide-field Imaging Survey Polarimeter* images and a large 4400 Å mosaic of Burrell Schmidt CCD frames. Dust thermal emission maps were extracted from *IRAS* data.

The scattering geometry analysis is complicated by the blending of light from many stars and the likely presence of more than one scattering layer. Despite these complications, we conclude that most of the scattered light comes from dust in front of the stars in at least two scattering layers, one far in front and extensive, the other nearer the stars and confined to areas of heavy nebulosity. The first layer can be approximated as an optically thin, foreground slab whose line-of-sight separation from the stars averages ~ 0.7 pc. The second layer is also optically thin in most locations and may lie at less than half the separation of the first layer, perhaps with some material among or behind the stars. The association of nebulosities peripheral to the main condensation around the brightest stars is not clear.

Models with standard grain properties cannot account for the faintness of the scattered UV light relative to the optical. Some combination of significant changes in grain model albedo and phase function asymmetry values is required. Our best-performing model has a UV albedo of 0.22 ± 0.07 and a scattering asymmetry of 0.74 ± 0.06. Hypothetical optically thick dust clumps missed by interstellar sightline measurements have little effect on the nebular colors but might shift the interpretation of our derived scattering properties from individual grains to the bulk medium.

[1]Dept. of Physics & Astronomy, University of Calgary, 2500 University Drive N.W., Calgary, Alberta T2N 1N4, Canada; gibson@ras.ucalgary.ca

[2]Dept. of Astronomy, University of Wisconsin, 475 N. Charter St., Madison, WI 53706; khn@sal.wisc.edu

Subject headings: scattering — methods: analytical — (ISM:) dust, extinction
— ISM: individual (Pleiades) — (ISM:) reflection nebulae — ISM: structure

1.   Introduction

Photometric studies of reflection nebulae have the potential to reveal the 3-D geometry
of diffuse interstellar clouds and the optical properties of their dust grains, but separating the
effects of geometry and grain scattering parameters is not straightforward. The difficulties are
most pronounced in the far-ultraviolet, where the observations are especially complex (e.g.,
Bowyer 1991; Henry 1991), and major disagreements remain over far-UV dust properties
(e.g., Hurwitz, Bowyer, & Martin 1991; Witt et al. 1992). Breaking the dust-geometry
degeneracy requires external constraints and careful analysis.

The Pleiades reflection nebula is a favorable case for such study, with a distance of order
100 pc (e.g., van Leeuwen 1999), large angular size, bright scattered light, and possibly simple
geometry. Except for the area of heaviest nebulosity near the star 23 Tau, the optical depth
of the nebula appears low ($E_{B-V} \sim 0.03 - 0.05$; see Breger 1986 and references therein), and
there is little other dust along the cluster sightline (Černis 1987). The wealth of structure in
the nebula (Arny 1977) may complicate photometric analysis. However, a Pleiades analysis
should be more reliable than the troubling examples posed recently by Mathis, Whitney, &
Wood (2002), given the nebula's many external geometric constraints (§2), low optical depth
along many sightlines, and lack of obvious extinction by clumpy dust (§4.2).

In the first paper in this series (Gibson & Nordsieck 2003; hereafter Paper I), we pre-
sented new wide-field imaging photometry of the Pleiades nebula at 1650 Å and 2200 Å with
the *Wide-field Imaging Survey Polarimeter* (*WISP*; Nordsieck & Harris 1999) and at 4400 Å
with the Burrell Schmidt telescope. It was found that phase function effects dominate over
internal reddening and that the UV/optical colors of the nebula are too red to explain with
common grain models.

Some prior investigations of the Pleiades (Greenberg & Roark 1967; Witt 1985) have
used only single-scattering models with attenuation to mimic internal extinction. Our pri-
mary analysis (§§3-5) adopts a similar strategy, with the added assumption of a geometrically
thin nebula to allow scattering along each sightline to be characterized by a single angle with
respect to a single star, though which star is used depends upon position. We also consider
a secondary analysis (§6) in which the single scattering approximation is retained but single
illuminators are not: blends of light from neighboring stars are represented explicitly.

2. Nebular Geometry Constraints

Interstellar absorption studies (e.g., Federman 1982; Bohlin et al. 1983; White 1984; White et al. 2001) and radio emission maps (e.g., Gordon & Arny 1984; Federman & Wilson 1984; Bally & White 1986) reveal both atomic and molecular gas in the Pleiades vicinity, at least some of which lies in front of the bright stars. Photometric colors indicate that foreground dust dominates the scattered light (Paper I). Most of the detected molecular gas is found in areas of heavy nebulosity on the west side of the cluster, especially southwest of the star 23 Tau, and it is accompanied by enhancements in interstellar polarization and reddening (White 1984; Breger 1986, 1987) as well as far-infrared emission (Castelaz, Sellgren, & Werner 1987; White & Bally 1993). Figure 1 shows the distributions of E_{B-V}, ^{12}CO emission, and optical brightness across the cluster core, which has a diameter of $\sim 2°$ (Adams et al. 2001). The foreground atomic gas displays at least two distinct velocity components. One of these outlines the general nebular structure, including features traced by the molecular gas, while the other extends over a much larger area and appears more smoothly distributed (Gordon & Arny 1984; White 1984). For convenience, we label the smooth, large-scale foreground feature as Component 1 and the more confined feature as Component 2. The limited angular extent of Component 2 suggests much of the Pleiades nebula may be reasonably characterized by a single scattering layer.

The gas kinematics indicate a state of collision with the cluster (Gordon & Arny 1984; White & Bally 1993; White 2002), while the multiplicity and spatial separation of velocity components (e.g., Gordon & Arny 1984; White 1984; White et al. 2001) suggest more than one cloud may be present. Component 1 appears situated ~ 1 pc in front of the cluster, with a sheetlike thickness of ≤ 0.3 pc (White 1984), in contrast to its many pc^2 area on the sky. Component 2 is estimated to lie much closer to or even among the stars (Breger 1987; White 1984; Freeman & Williams 1982; Federman 1982; Jura 1977, 1979), with an unknown sightline thickness, though the dominant scattering should arise from the portion in front of the stars for forward-scattering grains. An additional, weaker component appears in some absorption measurements (e.g., White & Bally 1993; White 2002). Its position and distribution along the line of sight are as yet poorly constrained.

Even with these complications, a single component could dominate the nebular intensity under the right conditions, such as one layer containing much more scattering material than the others or lying so that it scatters very efficiently at the positions observed. If no single layer dominates the scattered light, the geometry derived from observed intensities will instead represent a weighted average of the different components. We consider some general effects of multilayer scattering where it appears likely to occur (§§5-6).

3. Single Illuminator Model

Our primary model assumes only single scattering of light from a single star that is either the brightest in the vicinity or a fictitious illuminator mimicking the local radiation field. The model geometry is shown in Figure 2. The observed UV and optical intensity in each image pixel arises from a corresponding *parcel* of nebular dust. The same parcel is also heated by absorbed starlight to produce the observed far-infrared (FIR) thermal radiation. This simple representation has the advantage of being analytic, with well-understood constraints. Here we present mathematical details of the model. Results are discussed in the following two sections (§§4-5). Though the real nebula is lit by multiple stars as well as the general interstellar radiation field, the single-star analysis produces results that are consistent with a model incorporating these effects (§6).

There have been similar treatments of single scattering (e.g., Witt 1985). Ours differs in requiring the nebular extent along the sightline to be thin enough that scattering angles can be treated as constant within small areas on the sky. While less general, this approach yields a direct determination of geometric parameters. It also requires no detailed information on incident fluxes or the nebular optical depth distribution. Below we present an idealized version of the model followed by elaborations to explore the effects of smooth and clumpy internal extinction.

3.1. Zero Internal Extinction

The ideal case of zero internal extinction, or pure single scattering, is fully analytic. Since the dust is optically thin, each parcel intercepts a fraction of the incident starlight that translates into a sightline optical depth of $\tau_p(\lambda) = 0.4 \ln 10 \, (A_\lambda/A_V) \, R_V \, E_{B-V}$, where A_V and E_{B-V} are the total and selective extinction, and we describe the extinction curve A_λ/A_V by the empirical law of Cardelli, Clayton, & Mathis (1989), with $R_V \equiv A_V/E_{B-V}$ as a parameter.

The scattered intensity of the nebula, averaged over the instrumental bandpass, is

$$I_{\lambda_{scat}} \quad = \quad \frac{R_*^2}{r^2} \int_0^\infty F_*(\lambda) \, \tau_p(\lambda) \, a(\lambda) \, \Phi(\theta, \lambda) \, \xi_{scat}(\lambda) \, d\lambda \ , \tag{1}$$

where $I_{\lambda_{scat}}$ and $F_*(\lambda)$ are per unit wavelength and $F_*(\lambda)$ is the stellar surface flux from a Kurucz (1993) model of appropriate spectral type; the stellar radius R_* and star-parcel distance r convert $F_*(\lambda)$ into the proper intensity units. The grain albedo is $a(\lambda)$, $\Phi(\theta, \lambda)$ is

the scattering phase function, and $\xi_{scat}(\lambda)$ is the response function of the detector, normalized so that $\int_0^\infty \xi_{scat}(\lambda) \, d\lambda = 1$.

Large grains are heated to an equilibrium temperature T by absorption of the stellar flux and radiate thermally. Smaller grains undergo nonequilibrium heating and radiation. The combined FIR radiation of all grains, averaged over the detector bandpass, is given by

$$I_{\lambda_{FIR}} \quad = \quad \frac{R_*^2 \, \epsilon_{FIR}(T, \alpha)}{4\pi r^2} \int_0^\infty F_*(\lambda) \, \tau_p(\lambda) \, [1 - a(\lambda)] \, d\lambda \ . \tag{2}$$

Here $\epsilon_{FIR}(T, \alpha)$ is the fraction of the FIR radiation detected:

$$\epsilon_{FIR}(T, \alpha) \quad \equiv \quad f_{em}(T) \, \frac{\displaystyle\int_0^\infty B_\lambda(T) \, \tau_p(\lambda) \, \xi_{FIR}(\lambda) \, d\lambda}{\displaystyle\int_0^\infty B_\lambda(T) \, \tau_p(\lambda) \, d\lambda} \quad , \tag{3}$$

where $B_\lambda(T)$ is the Planck function, $f_{em}(T)$ is the fraction of the emission that can be represented by grains with temperature T, and $\xi_{FIR}(\lambda)$ is the response function of the detector (in this case, the *IRAS* 100 μm band). We assume the FIR opacity of the grains varies as $\lambda^{-\alpha}$ (e.g., Hildebrand 1983).

We estimate T as the *IRAS* 60/100 μm color temperature $T_{60/100}$, assuming $\alpha = 2$. This representation overestimates the large-grain temperature by a few K (Paper I) and also neglects significant FIR power from small grains at 12 & 25 μm (Castelaz et al. 1987). In the cluster core, a $T = T_{60/100}$ component reproduces $\sim 50\%$ of the DIRBE intensity integrated over $\lambda \sim 4 - 300$ μm, leaving a $\sim 15\%$ residual at longer wavelengths and a $\sim 35\%$ residual at shorter wavelengths. Since our analysis requires the superior resolution of *IRAS*, we estimate the total FIR emission by assuming a constant $f_{em}(T_{60/100}) = 0.5$ correction to the *IRAS* 60 & 100 μm data. Errors of a few percent in f_{em} may arise from spatial variations in dust temperature or uncertainties in zodiacal emission subtraction, but these should have little impact on our analysis. Even in the extreme case of $f_{em}(T_{60/100}) = 1.0$, the derived scattering angles are only $\sim 10 - 20°$ smaller than for $f_{em}(T_{60/100}) = 0.5$, and the UV scattering properties in the two cases are consistent within 1σ uncertainties.

The ratio of equations (1) & (2) cancels some scaling factors and yields a solution for $\Phi(\theta, \lambda)$, averaged over the photometric bandpass function $\xi_{scat}(\lambda)$ and weighted by the λ-dependence of the product $F_*(\lambda) \, \tau_p(\lambda) \, a(\lambda)$ within the band:

$$\langle \Phi(\theta, \lambda) \rangle_{\lambda_{scat}} \quad = \quad \frac{1}{4\pi} \left(\frac{I_{\lambda_{scat}}}{I_{\lambda_{FIR}}} \right) \epsilon_{FIR}(T, \alpha) \; h_{\mathrm{neb}} \;\; , \tag{4}$$

where the integrals describing the transmission of light through the nebula are collected as

$$h_{\mathrm{neb}} \quad = \quad \frac{\displaystyle\int_0^\infty F_*(\lambda) \, [1 - a(\lambda)] \, \tau_p(\lambda) \, d\lambda}{\displaystyle\int_0^\infty F_*(\lambda) \, a(\lambda) \, \tau_p(\lambda) \, \xi_{scat}(\lambda) \, d\lambda} \;\; . \tag{5}$$

The absolute scaling of τ_p cancels in the ratio, leaving only the form of the A_λ/A_V extinction curve. The stellar flux scaling also drops out, leaving only the spectral shape.

Equation (4) allows a direct measure of the phase function value. Since $I_{\lambda_{scat}}$ and $I_{\lambda_{FIR}}$ are observed quantities, F_* and T are constrainable by observation, and ξ_{scat} and ϵ_{FIR} are instrumental parameters, we can apply grain model values for A_λ/A_V, a, and α to equations (4) & (5) to obtain $\Phi(\theta)$. If the form of $\Phi(\theta)$ is known, this yields the scattering angle θ, hence 3-D nebular geometry. Conversely, a known geometry can be used to determine $\Phi(\theta)$'s behavior. We assume the Henyey & Greenstein (1941) form $\Phi_{HG}(\theta) = (1/4\pi)(1 - g^2)/(1 + g^2 - 2g\cos\theta)^{3/2}$, where the scattering asymmetry $g \equiv \langle \cos\theta \rangle$. The HG phase function probably represents real scattering poorly at large angles, but it may suffice for $\theta < 60°$ (Mathis 1990), and it is easily solved for θ.

Lastly, we use θ with the star-parcel offset angle ϕ seen by the observer to determine the 3-D position of each parcel relative to the illuminating star. Regardless of the overall nebular geometry, this parcel position is described by

$$\tan(\theta - \phi) \quad = \quad \left(\frac{d - s}{s} \right) \tan\phi \;\; , \tag{6}$$

where d is the star-observer distance, and s is the component of the star-parcel distance parallel to d. These relationships are illustrated in Figure 3. We assume $d = 130$ pc for our calculations, though the exact value remains under debate (Stello & Nissen 2001).

3.2. Smooth Internal Extinction

Since internal extinction may affect the nebular colors but we cannot model multiple scattering, we add smooth dust attenuation factors to the incident and scattered light terms of equation (5):

$$h_{\mathrm{neb}} \quad = \quad \frac{\displaystyle\int_0^\infty F_*(\lambda)\, e^{-\tau_1(\lambda)}\, \tau_p(\lambda)\, [1 - a(\lambda)]\, d\lambda}{\displaystyle\int_0^\infty F_*(\lambda)\, e^{-\tau_1(\lambda) - \tau_2(\lambda)}\, \tau_p(\lambda)\, a(\lambda)\, \xi_{scat}(\lambda)\, d\lambda} \quad . \tag{7}$$

Here τ_1 and τ_2 are the optical depths before and after the scattering/heating event; τ_2 does not apply for heating. This representation is valid as a first order approximation in the limit of zero albedo and zero heating outside of the scattering parcel. Since $\tau_p(\mathrm{opt}) \ll 1$ and our analysis in §4 finds low UV albedos, secondary scattering may be unimportant. The neglect of heating from τ_1 causes h_{neb} and Φ to be underestimated, but this bias may be small if $\tau_1(\mathrm{UV})$ is reasonably low.

We assume a simple face-on slab geometry and define the attenuation depths relative to the slab midplane, with $\tau_1 = \tau_p/[2\cos(\theta - \phi)]$ and $\tau_2 = \tau_p/(2\cos\phi)$. A similar treatment is given for smooth-dust reddening in Paper I. The inclusion of geometric terms in τ_1 and τ_2 requires that θ be obtained from equation (4) by iteration.

3.3. Clumpy Extinction

As outlined in Paper I and detailed in our analyses below, a smooth dust model with realistic input parameters has difficulty explaining the faintness of the Pleiades nebula in the ultraviolet with commonly-used grain (a, g) values. The internal reddening of a homogeneous foreground slab nebula is limited by the low interstellar reddenings observed toward the major Pleiades stars, and cannot by itself account for the observed nebular colors. However, the Pleiades nebulosity is filamentary on all observed scales (Arny 1977), extending down to subarcsecond resolution (Herbig & Simon 2001). Small dust filaments are also visible in other parts of the sky (e.g., Kalas et al. 2002) and may be fundamental to the nature of diffuse interstellar clouds.

Optically thick clumps of dust will act as a separate scattering population with lower effective albedo than the individual grains that compose them (Witt & Gordon 1996; White 1979b). Actual Pleiades clumps may cover a wide range of scales, shapes, and optical depths, but for simplicity we assume uniform clumps that are small compared to our model parcels. If these clumps are small and far apart, few stellar sightlines will intersect one, even though every parcel could contain many. No star in the Pleiades cluster should have an apparent diameter exceeding $\sim$0.001″, and thus the ratio of stellar disk area to the 3″.5×3″.5 solid angle resolution of smoothed *WISP* data will be less than 10^{-10}: millions of small dust clumps could lurk in each parcel and never occult a single bright star directly.

A thorough exploration of clumpy scattering in the Pleiades lies outside the scope of this paper. We assume that the clumps are completely absorbing for $\lambda < 3000\,\text{Å}$ and completely transparent otherwise, an extreme case that places a limit on clump reddening of the UV/optical colors. We define f_c as the fraction of light intercepted by clumps and generalize equation (7):

$$h_{\text{neb}} \;=\; \frac{\displaystyle\int_0^\infty F_*(\lambda)\,e^{-\tau_1(\lambda)}\,\left\{[1 - f_c(\lambda)]\,\tau_p(\lambda)\,[1 - a(\lambda)] \;+\; f_c(\lambda)\right\}\,d\lambda}{\displaystyle\int_0^\infty F_*(\lambda)\,e^{-\tau_1(\lambda) - \tau_2(\lambda)}\,[1 - f_c(\lambda)]\,\tau_p(\lambda)\,a(\lambda)\,\xi_{scat}(\lambda)\,d\lambda} \;. \tag{8}$$

The lack of obvious occultations by clumps in the Pleiades indicates f_c is probably small. In §4.2, we select a maximum likely value for $f_c(\text{UV})$ to assess the limits of clump reddening.

4. UV Dust Properties

In this section, we use the nebular photometry of Paper I and the single-star model of §3 to constrain properties of nebular illumination, dust extinction, reddening, and scattering. We require that scattering angle maps derived from the UV/FIR colors agree with those derived from the optical/FIR colors. This agreement implies nonstandard UV dust properties if standard grain models are assumed at optical wavelengths. The geometry of a nebular model with UV-altered dust is discussed in §5.

4.1. The Problem of UV Faintness

Given the predominantly foreground scattering, low sightline reddening, and blue colors of the brightest stars in the Pleiades, the redness of the nebular UV/optical colors (Paper I) is a serious constraint for scattering models. The left-side panels of Figure 4 illustrate the problem with scattering angle maps that agree poorly between our UV and optical photometric bands. The maps use the smooth-dust nebular model (§3.2) with Gordon, Calzetti, & Witt (1997; GCW) scattering properties, a B7III stellar spectrum, $R_V = 3.1$, and $E_{B-V} = 0.05$. Though all of these are reasonable choices based on available information, most of the derived UV scattering angles are larger than their optical counterparts by $\sim 20°$ or more. This discrepancy must be addressed with alternate models. The right-side panels of Figure 4 show a superior model, to which we will return in our discussion.

4.2. Parameter Space Search

Using equations (4) & (8), we computed scattering angles for $\lambda_{scat} = 1650$, 2200, and 4400 Å for a variety of parameter combinations to see which allow $\theta_{1650} \simeq \theta_{2200} \simeq \theta_{4400}$. The parameters explored were: the stellar input spectrum $F_*(\lambda)$; extinction parameter R_V, specifying a Cardelli et al. (1989) extinction curve; the sightline reddening E_{B-V}; the UV clump opacity $f_c(\mathrm{UV})$; the dust albedo $a(\lambda)$; and the scattering asymmetry $g(\lambda)$ used in the HG phase function. All of these properties were assumed constant over the nebula. Though E_{B-V} and the input spectrum vary with position, most of these variations are smaller than the parameter ranges we examined.

To optimize our search for the best model, we explored the two separate parameter grids summarized in Table 1. The primary grid varied $F_*(\lambda)$, R_V, E_{B-V}, and $f_c(\mathrm{UV})$ while using standard grain model $a(\lambda)$ and $g(\lambda)$ values for all wavelengths. Results from this grid demonstrate that standard UV (a, g) values are inadequate. The second grid used a few interesting (F_*, R_V, E_{B-V}, f_c) combinations from the first grid and varied $a(\lambda)$ and $g(\lambda)$ from their standard UV values. The two standard grain models used were Mathis, Rumpl, & Nordsieck's (1977; MRN) simple power-law size distribution of spherical grains, as explored by White (1979a) (Draine & Lee 1984 found similar results in our photometric bands), and GCW's compilation of diffuse dust results for the Milky Way. Standard MRN and GCW (a, g) values are given in Table 2.

The ranges of the explored parameters were set by observational constraints. Since the six brightest stars providing $\sim 2/3$ of the total light have B6-B8 III-IV spectra, the B7III spectrum of the brightest Pleiad, 25 Tau, is a representative cluster average. We also considered cooler B8III and B9III average spectra to redden the nebular colors, though these are less likely. Following Lang (1992), we used $T_{eff} = 13000$, 12500, and 11000 K and a surface gravity of $10^{3.5} \, \mathrm{cm \, s^{-2}}$ to specify the Kurucz (1993) models. Standard $R_V = 3.1$ extinction is consistent with estimates of $\sim 3 - 4$ for the Pleiades (e.g., Guthrie 1987; Witt, Bohlin, & Stecher 1981). Because a high R_V reduces the UV scattered intensity by flattening the extinction curve, we considered $R_V = 5$ as well, even though such nonstandard extinction is not strictly consistent with the MRN and GCW dust models. Apart from the heavy nebulosity SW of 23 Tau, reddenings are $E_{B-V} \sim 0.0 - 0.1$, averaging $0.03 - 0.05$ (Breger 1986). We allowed clump blocking fractions of $f_c(\mathrm{UV}) = 0.0 - 0.3$. Higher values are unlikely, since sightline blocking of less than $\sim 10^{-1}$ is implied by the lack of bright stars with anomalously large E_{B-V}, and blocking along the incident+scattered light path through the nebula is unlikely to be more than 2 or 3 times greater unless scattering angles are unrealistically large. "Gray" clumps with $\tau \gg 1$ and $E_{B-V} = 0$ may be present, but these would not affect the UV/optical colors. The second grid's UV (a, g) variations were

constrained by $g(\mathrm{UV}) > 0$ (Paper I).

We computed differences between UV and optical scattering angles, $\Delta\theta \equiv \theta_{\mathrm{UV}} - \theta_{\mathrm{opt}}$, for each model in both parameter grids, with the goal of finding models that minimize $|\Delta\theta|$. We used our own photometry as well as supplemental UV data from Witt, Bohlin, & Stecher (1986; WBS). Our general procedure for each model was: (1) compute $\Delta\theta_{ij\lambda}$ at position i in photometry set j (either WISP or WBS) for UV wavelength λ (1650 or 2200 Å); (2) extract a representative $\Delta\theta_{j\lambda}$ value for each set from these positional results; and (3) select the value $\Delta\theta = \mathrm{Max}\{|\Delta\theta_{j\lambda}|\}$ as the overall figure of merit for the model under consideration. This overall $\Delta\theta$ was then used to identify the most satisfactory models.

For our WISP and Schmidt data, we calculated the absolute mean difference $|\langle\Delta\theta_{ij\lambda}\rangle|$ for points within the $10' \times 10'$ box in Fig. 4. This box avoids point spread and other WISP image artifacts but has enough pixels (400) for a good statistical ensemble, and one that is representative of the bulk of $\Delta\theta_{ij\lambda}$ values over the area of Fig. 4. We chose $|\langle\Delta\theta_{ij\lambda}\rangle|$ over a more traditional root-mean-square $\langle(\Delta\theta_{ij\lambda})^2\rangle^{1/2}$ measure because the latter yields different ranges for data with different amounts of noise, such as the WISP 1650 & 2200 Å photometry, and normalizing these ranges by the error in $\Delta\theta_{ij\lambda}$ requires propagating the photometric errors through the inverted phase function, which is nontrivial. By contrast, $|\langle\Delta\theta_{ij\lambda}\rangle| \to 0$ whenever the average angles agree, and this statistic's insensitivity to different amounts of scatter merely leads to conservative constraints on the model parameter space, because fewer solutions are excluded than might be with an RMS analysis.

The WISP $10' \times 10'$ box has optical scattering angles exceeding $60°$ for standard GCW grains (Fig. 4). To include smaller angles in our scattering analysis, we computed representative $\Delta\theta_{j\lambda}$ values from the UV photometry of WBS, who observed at offsets of $20''$ and $40''$ from both 17 and 20 Tau and $20''$ and $60''$ from 23 Tau, implying $\theta =$ a few degrees. No other UV study has such small offsets; those of Andriesse et al. (1977) are similar to WISP's. Optical photometry at the WBS positions is not available in our Schmidt data or other studies, but we were able to estimate θ_{opt} from its value in the $10' \times 10'$ box and an assumed face-on slab geometry. IRAS photometry exists at the WBS positions, though it lacks structure on subarcminute scales. A more serious concern is the possibility of bias in the WBS photometry: their redder, more starlike colors at smaller offsets contradict other findings (Paper I; Andriesse, Piersma, & Witt 1977) unless the phase function is complex at small angles. But despite this possible bias, even approximate measurements at small angles are better than none. Still, the $\Delta\theta_{ij\lambda}$ values derived for each of the six WBS points often disagree with each other by $\sim 10°$ or more. The cause may be the geometric assumptions we used to infer optical photometry or perhaps some problem with the WBS photometry. Rather than attempt to average $\Delta\theta_{ij\lambda}$ over a few points with possible systematic errors, we

have used $\Delta\theta_{j\lambda} = \text{Min}\{|\Delta\theta_{ij\lambda}|\}$. As in the *WISP* analysis, this statistic is conservative: it minimizes the parameter space constraints and maximizes the range of acceptable models.

The model wavelength integrals were performed over a range of $1000 \leq \lambda \leq 10,000$ Å in steps of $\Delta\lambda = 50$ Å. Though limited by the tabulated MRN/GCW grain model data, this range includes our *WISP* and Schmidt passbands, and it misses only a few percent of the B7III stellar UV heating flux and even less for cooler spectra. Where $a(\lambda)$ and $g(\lambda)$ were allowed to vary in the UV, the MRN/GCW values were retained for $\lambda \geq 2600$ Å, while the properties for $1000 \leq \lambda < 1990$ Å and $1990 \leq \lambda < 2600$ Å were represented by (a_1, g_1) and (a_2, g_2), respectively. These parameters' wavelength ranges match the two *WISP* passbands, except the coverage of a_1 was extended to tie the shortest-wavelength UV heating in the model to observed scattered light properties.

4.3. Parameter Search Results

4.3.1. Fixed (a, g) Models

A thorough exploration of the primary grid demonstrated the inadequacy of the standard MRN and GCW grain model UV (a, g) properties. Although cooler stellar spectra and higher R_V, E_{B-V}, and $f_c(\text{UV})$ all help to reduce $|\Delta\theta|$, none of these can reduce it sufficiently, even in combination. The closest UV-optical match occurs for an unrealistically cool B9III spectrum with GCW grains, $R_V = 4.0$, $E_{B-V} = 0.05$, and $f_c(\text{UV}) = 0.30$, with $|\Delta\theta| = 2.3°$, where this is the larger of $|\theta_{1650} - \theta_{4400}|$ and $|\theta_{2200} - \theta_{4400}|$ for both *WISP* and WBS photometry. The best B7III and B8III GCW matches require $E_{B-V} = 0.10$ to achieve $|\Delta\theta| = 5°$; with a more realistic $E_{B-V} = 0.05$, such models have $|\Delta\theta| \geq 11°$. MRN grains perform worse than GCW grains. The best MRN models have $|\Delta\theta| \geq 10°$ even with $E_{B-V} = 0.10$. The poorer showing of MRN arises in part from its $g(2200) < g(4400)$ behavior, which contradicts the UV/optical color trends of Paper I. Alterations to the MRN/GCW UV (a, g) properties appear necessary to achieve $|\Delta\theta| < 5°$ for reasonable nebular models.

4.3.2. Variable (a, g) Models

Exploring UV (a, g) variations for all primary grid models was impractical, but we considered eight interesting cases, which we call Models A-H. These are listed in Table 3 along with the best UV (a, g) values found for each. Model A has the most likely nebular properties (§4.1), while the others illustrate various departures within the primary grid. Only two MRN cases met the minimum standard for acceptable solutions.

For each of these cases, $\Delta\theta$ values were computed over the UV (a, g) grid, with $|\Delta\theta| \leq 5°$ adopted as a criterion for acceptable solutions. The (a_1, g_1, a_2, g_2) explorations were performed separately for our photometry and the WBS data, each on (a_1, g_1, a_2) and (a_2, g_2, a_1) subspaces for efficiency; a_1 and a_2 are coupled in the heating integral and cannot be separated. After merging the *WISP* and WBS cubes by selecting the largest $|\Delta\theta|$ values in each, a full (a_1, g_1, a_2, g_2) 4-cube was constructed from the two 3-cubes by choosing the maximum $|\Delta\theta|$ at each position. Solutions with $g(\mathrm{UV}) < g(\mathrm{opt})$ were also eliminated to retain consistency with the Paper I color results. The average (a_1, g_1, a_2, g_2) values and standard deviations of the remaining solutions with $|\Delta\theta| \leq 5°$ are listed in Table 3.

The solution space is illustrated for the GCW Model A case in Figure 5. UV and optical scattering angle maps are shown in Figure 4 for this same case. θ_{UV} and θ_{opt} are in much closer agreement here than in the standard (a, g) case, both inside the $10' \times 10'$ box and in most areas outside, excluding *WISP* point spread artifacts. Specifically, we find the UV-modified GCW Model A case has $|\langle\Delta\theta\rangle| \sim 2°$ in the box for either *WISP* filter, with 1σ scatters of $\pm15°$ and $\pm7°$ about this mean for $|\langle\theta_{1650} - \theta_{4400}\rangle|$ and $|\langle\theta_{2200} - \theta_{4400}\rangle|$, respectively. The error in $|\langle\Delta\theta\rangle|$ is $\sigma/\sqrt{N}$, where the number of independent samples N allowed by angular resolution in the $10' \times 10'$ box is ~ 4 for the *IRAS* data and ~ 6 for the smoothed *WISP* data. The scattering angles in the box are also much lower than for standard GCW grains and are more likely to lie in the HG phase function's reliable range. Note that even if the WBS photometry were not used in our analysis, the set of *WISP*-based $|\Delta\theta| \leq 5°$ solutions excludes the standard GCW (a, g) properties.

The $a(\lambda)$ and $g(\lambda)$ plots in Figure 6 summarize all the models' behavior. Most MRN models have no solutions with $|\Delta\theta| \leq 5°$, which suggests problems even with the optical MRN (a, g) values. We find $g(\mathrm{UV})$ is slightly higher than standard GCW values and much higher than MRN. Conversely, $a(\mathrm{UV})$ is usually less than standard GCW values but agrees better with MRN for available solutions. Models with less smooth dust (A, C, E, & G) fall farther from standard (a, g) values. Our simplistic, extreme clumps make some MRN solutions possible and allow higher GCW albedo and g values, but real clumps will have less effect. The B7III and B8III solutions are very similar, since B8III is only slightly cooler. As in Paper I, we find no significant change in scattering properties between 1650 and 2200 Å. A slight 2200 Å albedo dip appears in some GCW models, and a $dg/d\lambda < 0$ trend occurs in all models, but both effects are within the error bars.

From this set, we selected GCW Model A as the best representation of the Pleiades dust. The only MRN models with viable (a, g) solutions require our overestimated clumpy dust extinction. Since real clumps would affect our results less, the smooth models offer a more economic description of the nebular extinction. Of the smooth GCW cases, Model A differs

more than the others from standard (a, g) values, but we feel the reduced (a, g) alterations of Models B, C, and D are not acceptable given these models' poor match to observed stellar spectra and R_V and E_{B-V} measurements. Figure 7 compares our GCW Model A choice against (a, g) values from other studies covering at least part of the *WISP* 1650 Å bandpass. If we ignore the possibility that scattering properties may differ between environments, our far-UV results show the greatest consistency with those of Sasseen & Deharveng (1996), Henry (2002), Murthy & Henry (1995), and Burgh, McCandliss & Feldman (2002), and the least consistency with Hurwitz et al. (1991), MRN, GCW, and Witt & Petersohn (1994).

Two caveats apply to our results. First, though our model clumps are not important for reddening, this does not mean clumps are not present. If clumps are common, our (a, g) properties may apply to the bulk medium rather than individual grains. Second, if multilayer scattering is significant in the regions we have examined, then the $g(\mathrm{UV}) > g(\mathrm{opt})$ trend (Fig. 6) will cause the average UV light to arise from dust farther in front of the stars than the average optical light, which in turn emerges in front of the isotropic thermal radiation. This wavelength separation of the average emitting regions could cause the UV faintness problem to be more severe, and the necessary (a, g) adjustments more extreme, because the sightline position of each wavelength's layer is that which maximizes the observed intensity. Thus, there is more FIR radiation relative to scattered light than the UV layer would produce, causing θ to be overestimated and the UV phase function to be sampled farther from its bright core than it should be. The θ_{opt} used as a reference for θ_{UV} will also be too large because the optical light scatters closer to the stars. If $d\Phi/d\theta < 0$ for $0° \leq \theta \leq 180°$ and $g > 0$, as the HG form implies, these arguments hold for background dust as well.

5. Scattering Geometry

We now discuss the geometry implied by the single-star scattering model parameters selected in §4. Using the optical data, which have the best quality, we examine the distribution of derived scattering angles and the implied 3-D geometry. We consider multistar and multilayer effects where appropriate. An alternative treatment of multistar scattering is given in §6.

5.1. Scattering Angles

Figure 8 shows an optical intensity map with optical scattering angle contours overlaid for the UV-modified GCW Model A case (Table 3). Most bright nebulosities in the map have

forward-scattering angles of $\theta < 90°$. Actual foreground dust requires $\theta - \phi < 90°$ (Fig. 3), but usually $\phi \ll \theta$. Consistent with the foreground geometry picture, we find smaller angles near bright stars. The lowest scattering angles occur in the main nebular condensation and near a handful of outlying stars, while higher angles trace weaker, more extended features. A prominent exception is the apparent backscattering southwest of 23 Tau. Background dust could be present here, but our calculations might also be compromised by optically thick dust (§2). In other regions with $\theta > 90°$, the scattered intensity from foreground dust may be less than that from the diffuse Galactic background. The exact extent of forward- vs. backscattering regions may differ from that shown in Fig. 8 if the HG phase function we have assumed is not appropriate for large angles.

Though θ is generally low near bright stars, it also tends to be higher on the west side of the cluster core than the east, implying larger scattering angles where there is more nebulosity. Representative values are $\theta \sim 60°$ near 17 Tau, $40°$ near 20 & 23 Tau, $30°$ near 25 Tau, and $20°$ near 27 Tau. What might cause this $40°$ change?

1. Spatial variations in dust properties are not sufficient. Our UV-modified GCW models (Table 3) can only produce $20°$ of variation, and then only if Model D conditions obtain near 17 Tau and Model E conditions obtain near 27 Tau. The real range is probably lower unless large, abrupt changes in dust properties are possible.

2. If more than one star illuminates the nebular parcel, the derived θ becomes a flux-weighted average over θ_i values for each contributor, where θ_i is larger for more distant stars, raising $\langle \theta \rangle$. This effect may explain why $\theta \neq 0°$ near bright stars, and multistar illumination seems more likely on the west side of the cluster. However, calculations in §5.2 using a partial multistar representation still produce a prominent east-west θ trend.

3. The θ trend could reflect real geometry. As a single sheet, the nebula might lie farther from the stars on the east side of the cluster than on the west. With a multilayer nebula, the outer layers could dominate on the east side, while the inner layers dominate on the west; in the naming scheme of §2, these would be Components 1 and 2, respectively.

The geometric interpretation would also predict lower dust temperatures on the east side than on the west. The 60/100 μm color temperature is significantly lower near 27 Tau than near 17, 20, or 23 Tau (Paper I; White & Bally 1993). Near 25 Tau it is comparable to 17, 20, and 23, but 25 Tau is also more luminous, which could compensate for a larger separation.

One complication for this picture is that E_{B-V}, which is supposed to trace nebulosity and larger θ values, is lower toward 17 Tau (0.020) than 27 Tau (0.031; Breger 1986). But the true geometry is unlikely to have all the stars behind all the dust. 17 Tau could lie in front of Component 2 and close to Component 1, thus having low E_{B-V} but high θ; absorption line evidence (White 1984) suggests 17 Tau is in front of most of the other bright stars. 27 Tau could lie at a somewhat larger distance than the other stars, reducing θ from its expected level.

5.2. Star-Nebula Separations

Figure 9 plots star-nebula separations along the line of sight, computed from the scattering angles θ of Fig. 8 with $s = d \tan \phi / [\tan \phi + \tan (\theta - \phi)]$ (eq. [6]; Fig. 3). The offset angle ϕ required for this calculation is easily measured for a single star, but for multiple illuminators, a representative value must be assumed. Though our model is designed only for the single-star case, we have bent this rule slightly to estimate ϕ and consider the implied 3-D geometry.

5.2.1. Offset Estimation

We estimated ϕ by two methods with different simplifying assumptions. These approaches give complementary information and provide useful checks on each other.

The *dominant star* method uses the closest bright star as the sole illuminator. We determine which star's light is dominant at each pixel in our map by assuming the stars and dust lie in the same plane normal to the line of sight and computing the flux contributions of all the stars at each position. Though very simple, this nebular model suffices for dominant star determination (e.g., Paper I); separating the stars and dust into different planes does not alter the results significantly unless the plane separation is unreasonably large. We use all Schmidt mosaic stars brighter than $B \sim 11$ regardless of cluster membership status, since some nebulosities may not be lit by cluster stars. Even so, most of the total light is provided by known cluster members.

The *average star* method calculates the average offset angle of the illuminating stars at each point weighted by the contributed flux of each star, i.e.,

$$\langle \phi(x,y) \rangle \quad = \quad \frac{\sum\limits_{i=1}^{N_*} 10^{-0.4\,B_i}\, r_i^{-2}(x,y)\, \phi_i(x,y)}{\sum\limits_{i=1}^{N_*} 10^{-0.4\,B_i}\, r_i^{-2}(x,y)} \quad , \tag{9}$$

where the model has N_* stars, and star i has apparent magnitude B_i as seen from Earth and lies at an incident path distance $r_i(x,y)$ from sightline position (x,y) in the nebula at offset angle $\phi_i(x,y)$ (see Fig. 3). Since the flux weights are normalized, the absolute flux of each star is not needed. We cannot obtain $r_i(x,y)$ rigorously without detailed knowledge of the 3-D geometry, but as a simple exercise, we assume a plane of stars shining on a plane of dust, both perpendicular to the sightline. The distance S between the two planes is a free parameter, and the derived offsets $\langle \phi(x,y) \rangle$ and separations $s(x,y)$ are both functions of S. However, most plane separations cause $s(x,y)$ to increase or decrease drastically near bright stars. Only a narrow range of S produces the relatively flat $s(x,y)$ behavior expected for a sheet of dust, and this range is generally consistent with the $s(x,y)$ values obtained.

5.2.2. Core Nebula Structure

For both offset estimation methods, we find lower separations around 17, 20, & 23 Tau on the cluster core's west side and higher separations around 25 & 27 Tau on the east, which is consistent with the east-west θ trend tracing closer scattering material on the west side than the east. Part of the trend could arise from starlight blending effects rather than real geometry (§5.1), since the average-star method only accounts for such effects in ϕ, not θ. But external constraints (§2) imply that much of the trend results from real geometry.

Though the dominant-star and average-star separations both have an east-west trend, they differ in other respects. The dominant-star method can produce discontinuities of a few tenths of a parsec between the domains of different stars, and its assumption of purely local illumination causes separations to be underestimated near bright stars because θ is larger than expected. The average-star method does not produce discontinuities, but its assumption that all the stars lie in the same plane maximizes the contributions of distant illuminators, causing separation enhancements near some stars. Consequently, the two methods represent extreme cases, with the average-star separations being larger than the dominant-star separations: respective values of $0.15 - 2.0$ pc and $0.05 - 1.0$ pc are found in the area between 17 and 27 Tau. The real nebular geometry is probably an intermediate case with intermediate separations.

5.2.3.   Peripheral Features

Our analysis has difficulty with the nebulosities outside the central region. Dominant-star separations drop and average-star separations rise near several bright stars, including HD 23753, 24118, 24178, 24213 and 24368. The average-star separations are better behaved around HD 23985, but this nebulosity is harder to explain physically: though long noted (Barnard 1900), it is associated with a star lying well inside the Local Bubble (ESA 1997; Sfeir et al. 1999) with no detected interstellar Na I absorption (White et al. 2001).

The limitations of both offset estimation methods are probably more severe for peripheral features. The average-star assumption that all stars lie at the cluster distance is less likely to apply to the outer nebulosities. HD 23753 is a cluster member, but it may be offset in distance from the core stars, while HD 24368 is in the near-background at 1.2 times the cluster distance (ESA 1997). The illuminating roles of the non-member stars HD 24118, 24178, and 24213 are uncertain, since all have nebular glows compact enough to be point spread artifacts. The dominant-star assumption of only local illumination may also be problematic if the ambient interstellar radiation field is important, as the optical/FIR colors suggest in the outer nebula (Paper I). Finally, both methods may suffer if the Henyey-Greenstein phase function is inappropriate for large-angle scattering, since this could significantly affect the balance of local vs. nonlocal illumination. Because of these limitations, the association of peripheral features with the central nebula remains unclear.

6.   Multiple Illuminator Analysis

Our secondary analysis considers the blending of light from multiple stars explicitly. The nebula is still assumed to be optically and physically thin, but the brightness at each point is now a function of many illuminators, each at its own distance and scattering angle. As a result, the 3-D geometry cannot be obtained from scattered/thermal intensity ratios and dust parameters. Instead, it must be assumed with the dust properties a priori and evaluated by comparing the resulting intensity maps against observations.

This intensity-based approach complements the single-star color analysis of §§3-5. The parameter space of possible geometries is vast, so only a few simple cases can be explored. However, multistar illumination effects are represented more accurately in these cases. Absolute stellar flux scalings and nebular opacities can also be examined since, unlike the single-star model, this model is sensitive to them. Model details and results are given below.

6.1. Model

We generalize the scattered light and thermal radiation integrals of §3:

$$I_{\lambda_{scat}} = I_{bg}(\lambda_{scat}) + R_*^2 \int_0^\infty \sum_{i=1}^{N_*} \frac{b_i\, F_*\, e^{-\tau_1-\tau_2}}{r_i^2} \left[1 - f_c\right] \tau_p\, a\, \Phi(\theta_i)\, \xi_{scat}\, d\lambda \qquad (10)$$

$$I_{\lambda_{FIR}} = I_{bg}(\lambda_{FIR}) + \frac{R_*^2\, \epsilon_{FIR}(T,\alpha)}{4\pi} \int_0^\infty \sum_{i=1}^{N_*} \frac{b_i\, F_*\, e^{-\tau_1}}{r_i^2} \left(\left[1 - f_c\right] \tau_p\, \left[1 - a\right] + f_c\right) d\lambda \ , \ (11)$$

where the λ-dependencies of the integrated variables have been dropped for clarity, and the stellar contributions are summed over the number of stars N_*. The set of stars is that used in §5.2.1. We assume all stars have the same spectrum but different luminosities $L_{*i} = b_i L_*$, where $L_* = 4\pi R_*^2 F_*$ is the standard luminosity for a star of the chosen spectral type, $b_i \equiv 10^{-0.4\Delta B_i}$, and ΔB_i is the catalog magnitude difference between 25 Tau and star i. As before, we use Kurucz (1993) surface fluxes for F_*. We interpolate R_* from Lang (1992) as $R_{\mathrm{B7III}} = 7.0\,\mathrm{R}_\odot$ and $R_{\mathrm{B8III}} = 6.5\,\mathrm{R}_\odot$. The HG form is used for Φ, and the parameters $F_*(\lambda)$, R_V, E_{B-V}, $f_c(\mathrm{UV})$, $a(\lambda)$, and $g(\lambda)$ are taken from the UV-modified GCW Models A-H of Table 3. The background intensity level I_{bg} is determined experimentally.

We adopt a simple geometry in which the dust and stars lie in separate planes normal to the line of sight, with the separation s as a free parameter. Like the average-star offset method in §5.2, this approach may overestimate starlight blending. The model can be generalized to multilayer scattering by summing over multiple dust planes, which we consider briefly in §6.2.3. For a single dust plane, θ_i is found from d, s, and ϕ_i with equation (6), the star-parcel distance is $r_i = s\,/\cos(\theta_i - \phi_i)$, and optical depths are given by the τ equations in §3. The dust plane's uniform optical depth may reasonably represent that of the smooth, distant Component 1 layer (§2). Though optical depth variations are clearly present, general brightness trends near stars (Paper I) indicate the importance of a smooth component, and deviations from such behavior can be used to map structure.

The total absorbed flux at each position is used to find the cluster-induced dust temperature T_{cl} via the Stefan-Boltzmann relation. To include heating from the general background field, we calculate the overall temperature as $T = T_{cl} + T_{bg}$, where $T_{bg} \sim 20\ K$ is the typical background level away from the cluster core. Physically, such temperatures should be summed as $T^{4+\alpha} = T_{cl}^{4+\alpha} + T_{bg}^{4+\alpha}$ for grains with emissivity power-law exponent α, but the larger range afforded by the linear sum is a better match to the $IRAS$ $60/100\ \mu$m color temperatures used in §§3-5, which have some small-grain bias (Paper I). Consistent input

temperatures allow a more straightforward comparison of our multistar and single-star results. Remaining differences in T between the multistar model and real nebula are much less important than likely differences in opacity structure or geometry.

6.2. Results

6.2.1. Intensity Zero-Level

If the model is lit only by the Schmidt field stars, it falls significantly short of observed brightness $\gtrsim 1°$ from the cluster center. A non-plane-parallel model could address this problem by shifting the peripheral dust far forward of the bright core stars to scatter more light at small angles, but such a solution is not very satisfactory (§5.2). Instead, we retained the plane-parallel geometry and added a constant background level to represent illumination from the general interstellar radiation field. This mechanism allows reasonable matches to observed intensities in the outer nebula, indicating the importance of external illumination in these areas. The exact background levels depend somewhat on the multistar model parameters, including the shape of the phase function for large-angle scattering. For the GCW Model A case adopted below, we find $I_{bg}(4400 \text{ Å}) \sim 3 \times 10^{-19} \text{ erg cm}^{-2} \text{ s}^{-1} \text{Å}^{-1} \text{arcsec}^{-2}$ = 25.9 B mag arcsec^{-2} and $I_{bg}(100 \ \mu\text{m}) \sim 5 \text{ MJy sr}^{-1}$. The *WISP* sensitivity is insufficient to estimate meaningful UV levels. However, the optical level is similar to that found for ambient cirrus clouds (e.g., Paley et al. 1991).

6.2.2. Nebular Parameters

We compared the multistar model to the observed nebula for all eight UV-modified GCW parameter sets in Table 3. The model performance is consistent with our §4.3 results. For the right choices of star-dust separation and background intensity, Models A and E both perform quite well: their UV and optical intensities are within a few tens of percent of observed levels over most of the nebula. The FIR intensities of the model also agree with the real nebula on average, though localized disagreements occur where the real dust column differs from that in the model. Models C and G perform adequately, but their fainter B8III illumination is a poorer match to the nebular brightness than the B7III illumination of Models A and E. At the same time, the increased amount of smooth dust in Models B, D, F, and H makes them overbright relative to the real nebula. A side test of Model A with the standard GCW UV properties matches the optical and FIR nebula but is overbright in the UV, reconfirming the need for UV-modified (a, g) properties. Since the UV-modified GCW

Model A has R_V and E_{B-V} values consistent with measurements and no ad hoc absorbing clumps, it is the subject of the remaining discussions.

6.2.3. Scattering Geometry

The star - dust separation s was varied to find the best match to observed intensities. The model's average intensity changes little with s, but its intensity distribution is sensitive to s, particularly near bright stars. Optimal s values produce observed/model intensity ratios that are near unity and relatively constant over large areas. If the basic picture of §2 is correct, the s found for most of the nebula will be that of Component 1. Where $E_{B-V} \lesssim 0.05$, we find a Model A Component 1 foreground separation of $s \sim 0.7$ pc for the optical data. Consistent values apply at UV and FIR wavelengths, though with greater uncertainty.

The separation maps of §5.2 match this $s \sim 0.7$ pc value in places, but they are probably less reliable for determining the position of Component 1, since the single-star approach cannot model starlight blending effects fully. Nevertheless, single-star scattering angles derived from the intensity maps of this multistar model do agree on average with those found from the observations for $\theta \lesssim 60°$, indicating a general consistency between the two models apart from some structural effects discussed below.

A discrepancy occurs for $\theta \gtrsim 60°$ however. The area around the central nebula with $\theta < 90°$ is about twice as large when derived from the multistar model intensities instead of observed intensities. A likely explanation is that real grains scatter less efficiently than the adopted Henyey-Greenstein phase function at large angles. If, for example, the multistar model's phase function is changed to $\Phi' = [\epsilon_{HG} | \cos \theta | + (1 - \epsilon_{HG})] \Phi_{HG}(g, \theta)$, the best match to the $\theta = 90°$ contours of Fig. 8 is provided by a 90° scattering decrement of $\epsilon_{HG} \sim 0.7$. The Φ' form is ad hoc, and the exact correction depends upon the adopted background intensity level, but $\epsilon_{HG} > 0$ seems necessary. Since our single-star analysis assumes $\Phi = \Phi_{HG}$, §5 may overestimate scattering angles and underestimate separations, and more nebulosity may lie in front of the stars than Fig. 8 indicates.

Figure 10 compares UV-modified GCW Model A intensities to the observed nebula at 4400 Å and 100 μm, using background levels from §6.2.1, $s = 0.7$ pc, and the above correction to Φ_{HG}. Differences between the model and observations arise from real 3-D geometry and dust structure not included in the model. If the model primarily represents Component 1, this residual structure traces the influence of Component 2, which has a greater optical depth than Component 1 and lies closer to the stars. Both effects will increase observed/model

ratio, so they are difficult to separate. For example, the west side of the cluster core has more dust (§2) at smaller separations (§5).

Because of this degeneracy, the separation of Component 2 is more difficult to estimate with the multistar model. If the observed/model ratio structure is assumed to be purely geometric, applying the same Model A nebula to the areas near 20 and 23 Tau gives $s \sim$ 0.35 pc at 4400 Å and $s \sim 0.25$ pc at 100 μm. These are lower limits if there is only one scattering layer. But in multilayer scattering, the separations are weighted averages, and the inner layer(s) could lie closer to the stars. Multiple layers could also explain the discrepancy between optical and FIR separations in this region if phase function effects cause the average radiation to emerge from different layers depending on wavelength (§4.3.2), or if the dust is thick to UV photons, which would cause a similar differentiation.

Our analyses assume a physically thin scattering layer to restrain θ on each sightline. We tried testing this assumption by summing thin models to simulate thick slabs, but this approach has large uncertainties: even in areas where Component 1 dominates the scattering, we can only constrain the slab thickness to $\lesssim 0.6$ pc at the 1σ level. White (1984) is more successful, finding a Component 1 thickness of $\lesssim 0.3$ pc, which restricts θ sufficiently in a nebular parcel for our models to be reasonably valid where Component 2 is not important.

6.2.4. Nebular Structure

High observed/model intensity ratios may be used as a proxy to map Component 2 over the cluster area. Many high ratios are found on the west side of the cluster core, especially SW of 23 Tau. The ratios in this area correlate to some degree with the E_{B-V} and $\tau(100\ \mu\text{m})$ tracers of nebular opacity, though significant scatter is introduced by *IRAS* noise and 3-D geometry details not included in the model. Conversely, low ratios trace reduced nebulosity, particularly in a region extending east from the environs of 25 Tau. This feature corresponds with a dust cavity identified by White & Bally (1993) in the *IRAS* data. The cavity's outlines are visible in intensity maps but more conspicuous in the ratio maps, which also show that the 20′ diameter hole in the optical nebulosity $\sim 1°$ NE of 25 Tau (Paper I) is part of a larger structure.

White & Bally (1993) posit that local density in the dust cavity has been lowered by photoelectric heating or radiation pressure, and (Gordon & Arny 1984) consider similar mechanisms to explain a counterpart hole in the neutral hydrogen 21cm emission. Figure 11 shows optical and FIR ratios overlaid with contours of our own H I 21cm data at a velocity tracing Component 2 (S. J. Gibson, in preparation). The H I associates with high ratios

near the cluster core and has a cavity similar to the dust cavity. These 21cm observations and higher-resolution synthesis maps will be presented in subsequent papers.

7. Conclusions

We have examined dust scattering in the Pleiades reflection nebula with some simple geometric models. We find the following results:

1. As implied by the color trends of Paper I, the dust dominating the scattering lies in front of the stars.

2. On average, the dust is closer to the stars on the west side of the cluster core than on the east, and greater optical depths occur on the west side. A multilayer geometry is likely, with one widespread layer ~ 0.7 pc in front of the stars and a second layer confined to areas of heavier nebulosity at half this distance or less; part of the second layer may even lie among or behind the stars. The first layer is probably optically thin, while the second may be optically thick in some areas.

3. The blending of incident light from multiple stars has a significant effect on the nebular brightness distribution. Our multistar model reproduces brightness trends near most stars quite well and is a useful tool for revealing nebular structures.

4. Real scattering efficiencies at angles approaching $90°$ may be less than those given by a Henyey-Greenstein phase function. Geometric analyses using HG functions may contain biases from poorly represented large-angle scattering.

5. Outlying nebulosities $1 - 2°$ from the cluster core may not receive the majority of their light from the core stars, but instead from other stars in the vicinity or from the general interstellar radiation field. The geometric association of these areas with the central nebula is unclear.

6. Available constraints suggest the ultraviolet faintness of the nebula is due to a mixture of lower UV albedo and greater forward-throwing of the UV phase function than standard grain models provide. Our best-performing model uses Gordon et al. (1997) Milky Way dust (a, g) properties modified to $(a = 0.22 \pm 0.07, g = 0.74 \pm 0.06)$ for $\lambda < 2600$ Å.

7. Clumpy dust does not affect the nebular colors significantly. But clumps might still be common. If so, our (a, g) values may apply to the bulk medium, not to individual dust grains.

More detailed results will require Monte Carlo modeling, which involves many more free parameters to describe the 3-D distributions of stars and dust. Accurate estimates of these input quantities will not be obtained easily, but they are essential to overcome the limitations of the current models, such as the plane-parallel geometry of §6. A major asset would be true 3-D positions of all the major stars, as future space-based trigonometric parallax missions may provide. For example, the *GAIA* mission's anticipated 1σ precision of 4 microarcseconds for bright stars (Perryman et al. 2001), or ~ 0.07 pc at the Pleiades distance, is equivalent to $\sim 1/10$ the typical angular separations of the brightest cluster stars.

An additional asset would be polarimetric imaging of the entire nebula as *WISP* originally intended, since this would help to disentangle the light contributions from different stars, particularly in the outer areas where the geometry is most ambiguous. A major ground-based imaging campaign might achieve the desired sensitivity for such work, but the optical polarimetric background is highly uncertain (Nordsieck et al. 1994). A space-based UV mission would avoid this problem, but the faint UV/optical nebular colors of the nebula (Paper I) require a sensitivity at least 10^3 times better than *WISP* and a greatly reduced point spread function.

REFERENCES

Adams, J. D., Stauffer, J. R., Monet, D. G., Skrutskie, M. F., & Beichman, C. A. 2001, AJ, 121, 2053

Andriesse, C.D., Piersma, Th.R., & Witt, A.N. 1977, A&A, 54, 841

Arny, T. 1977, ApJ, 217, 83

Bally, J., & White, R. E. 1986, in Proc. Summer School on Interstellar Processes: Abstracts of Contributed Papers, ed. D. J. Hollenbach & H. A. Thronson, Jr. (Washington: NASA TM, 88342), 51

Barnard, E. E. 1900, MNRAS, 60, 258

Bohlin, R. C., Hill, J. K., Jenkins, E. B., Savage, B. D., Snow, T. P. Jr., Spitzer, L. Jr., & York, D. G. 1983, ApJS, 51, 277

Bowyer, S. 1991, ARA&A, 29, 59

Breger, M. 1987, ApJ, 319, 754

Breger, M. 1986, ApJ, 309, 311

Burgh, E. B., McCandliss, S. R., & Feldman, P. D. 2002, ApJ, 240

Cardelli, J. A., Clayton, G. C., & Mathis, J. S. 1989, ApJ, 345, 245

Castelaz, M. W., Sellgren, K., & Werner, M. W. 1987, ApJ, 313, 853

Černis, K. 1987, Ap&SS, 133, 355

Draine, B. T., & Lee, H. M. 1984, ApJ, 285, 89

European Space Agency 1997, The Hipparcos Catalogue, ESA SP-1200 (Noordwijk: ESA)

Federman, S. R. 1982, ApJ, 253, 601

Federman, S. R., & Willson, R. F., 1984, ApJ, 283, 626

Freeman, A., & Williams, D. A. 1982, Ap&SS, 83, 417

Gibson, S. J., & Nordsieck, K. H. 2003, ApJ, accepted (Paper I)

Gordon, K. D., Calzetti, D., & Witt, A. N. 1997, ApJ, 487, 625 (GCW)

Gordon, K. J., & Arny, T. T. 1984, AJ, 89, 672

Greenberg, J. M., & Roark, T. P. 1967, ApJ, 147, 917

Guthrie, B. N. G. 1987, QJRAS, 28, 289

Henry, R. C. 2002, ApJ, 570, 697

Henry, R. C. 1991, ARA&A, 29, 89

Henyey, L. G., & Greenstein, J. L. 1941, ApJ, 93, 70

Herbig, G. H., & Simon, T. 2001, AJ, 121, 3138

Hildebrand, R. H. 1983, QJRAS, 24, 267

Hurwitz, M., Bowyer, S., & Martin, C. 1991, ApJ, 372, 167

Jura, M. 1979, ApJ, 231, 732

Jura, M. 1977, ApJ, 218, 749

Kalas, P., Graham, J. R., Beckwith, S. V. W., Jewitt, D. C., & Lloyd, J. P. 2002, ApJ, 567, 999

Kurucz, R. L. 1993, *The 1993 Kurucz Stellar Atmospheres Atlas* (Kurucz CD-ROM No. 13), available online from the Harvard-Smithsonian Center for Astrophysics (kurucz.harvard.edu)

Lang, K. R. 1992, *Astrophysical Data: Planets and Stars* (New York: Springer-Verlag)

Mathis, J. S. 1990, ARA&A, 28, 37

Mathis, J. S., Rumpl, W., & Nordsieck, K. H. 1977, ApJ, 217, 425 (MRN)

Mathis, J. S., Whitney, B. A., & Wood, K. 2002, ApJ, 574, 812

Murthy, J., & Henry, R. C. 1995, ApJ, 448, 848

Nordsieck, K. H., & Harris, W. M. 1999, *Proceedings of the Society of Photo-Optical Instrumentation Engineers (SPIE)*, 3764, 124

Nordsieck, K. H., Marcum, P., Jaehnig, K. P., & Michalski, D. E. 1994, *Proceedings of the Society of Photo-Optical Instrumentation Engineers (SPIE)*, 2010, 28

Paley, E. S., Low, F. J., McGraw, J. T., Cutri, R. M., & Rix, H.-W. 1991, ApJ, 376, 335

Perryman, M. A. C., et al. 2001, A&A, 369, 339

Sasseen, T. P., & Deharveng, J.-M. 1996, ApJ, 469, 691

Schiminovich, D., Friedman, P. G., Martin, C., & Morrissey, P. F. 2001, ApJ, 563, L161

Sfeir, D. M., Lallement, R., Crifo, F., & Welsh, B. Y. 1999, A&A, 346, 785

Stello, D., & Nissen, P. E. 2001, A&A, 374, 105

van Leeuwen, F. 1999, A&A, 341, L71

Weingartner, J. C., & Draine, B. T. 2001, ApJ, 548, 296

White, R. E. 2002, ApJ, submitted

White, R. E. 1984, ApJ, 284, 685

White, R. E., Allen, C. L., Forrester, W. B., Gonnella, A. M., & Young, K. L. 2001, ApJS, 132, 253

White, R. E., & Bally, J. 1993, ApJ, 409, 234

White, R. L. 1979b, ApJ, 230, 116

White, R. L. 1979a, ApJ, 229, 954

Witt, A. N. 1985, ApJ, 294, 216

Witt, A. N., Bohlin, R. C., & Stecher, T. P. 1986, ApJ, 302, 421 (WBS)

Witt, A. N., Bohlin, R. C., & Stecher, T. P. 1981, ApJ, 244, 199

Witt, A. N., Friedmann, B. C., & Sasseen, T. P. 1997, ApJ, 481, 809

Witt, A. N., & Gordon, K. D. 1996, ApJ, 463, 681

Witt, A. N., & Petersohn, J. K. 1994, *Ast. Soc. Pacific Conf. Ser.*, **58**, *The First Symposium on the Infrared Cirrus and Diffuse Interstellar Clouds*, eds. R. Cutri & W. Latter, 91

Witt, A. N., Petersohn, J. K., Bohlin, R. C., O'Connell, R. W., Roberts, M. S., Smith, A. M., & Stecher, T. P. 1992, ApJ, 395, L5
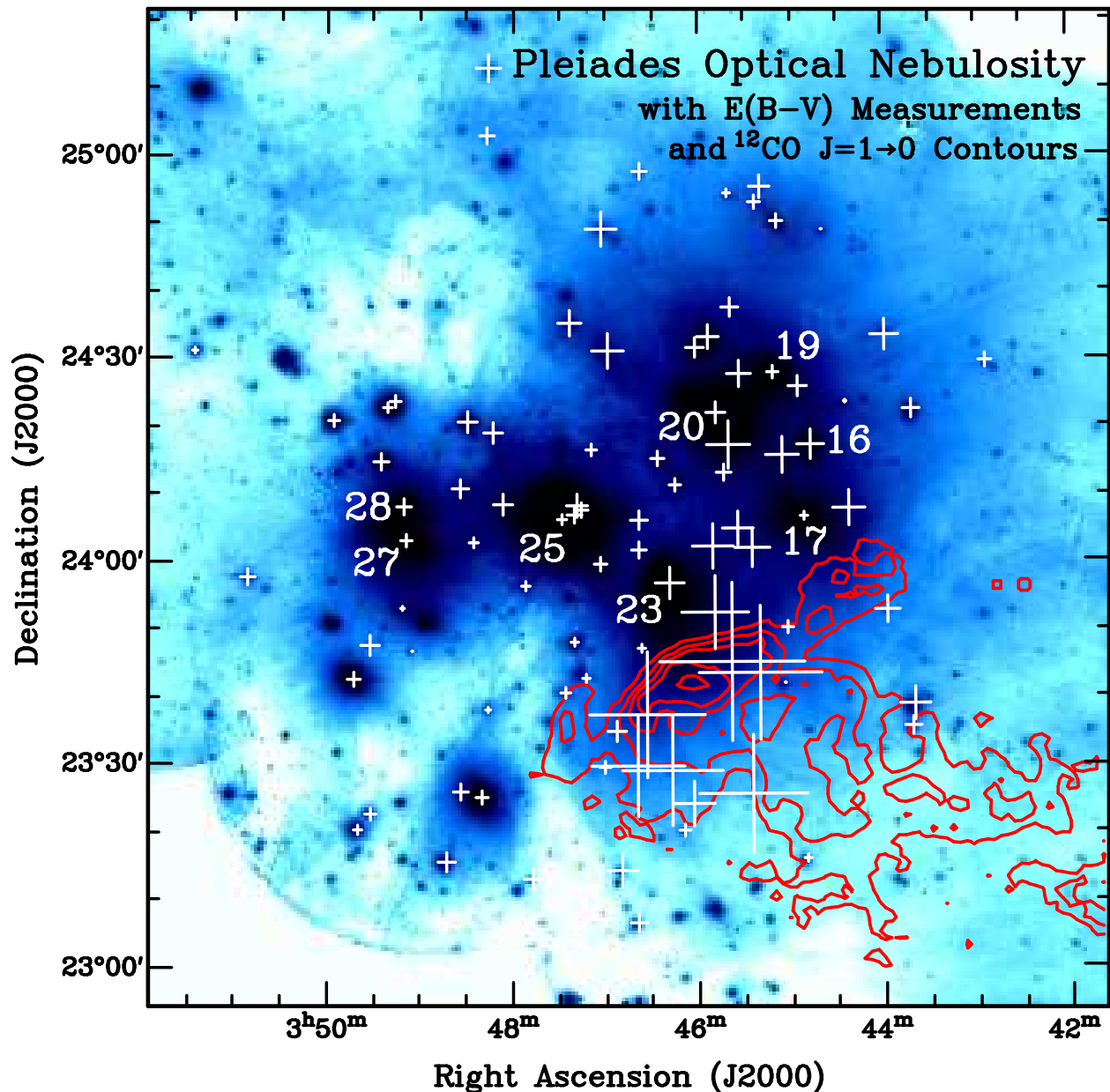
Fig. 1.— Interstellar reddening and molecular gas across the cluster core. Bright Flamsteed stars are numbered. The background is a log-scale negative image of 4400 Å nebulosity from Paper I, with intensities of $2.0 \times 10^{-19} - 2.0 \times 10^{-17}$ erg cm^{-2} s^{-1} Å^{-1} arcsec^{-2}, or $26.3 - 21.3$ B mag arcsec^{-2}. Crosses show reddenings toward cluster members (Breger 1986), where E_{B-V} = cross width in degrees. The contours mark 5, 10, 15, 20, and 25 K km s^{-1} profile integrals of ^{12}CO $J = 1 - 0$ emission from Bell Labs 7m telescope data provided by J. Bally & R. E. White (see Bally & White 1986). CH$^+$ absorption is also detected toward a number of stars, with larger column densities measured for 16, 20, & 23 Tau than for 19, 25, & 27 Tau (White 1984).
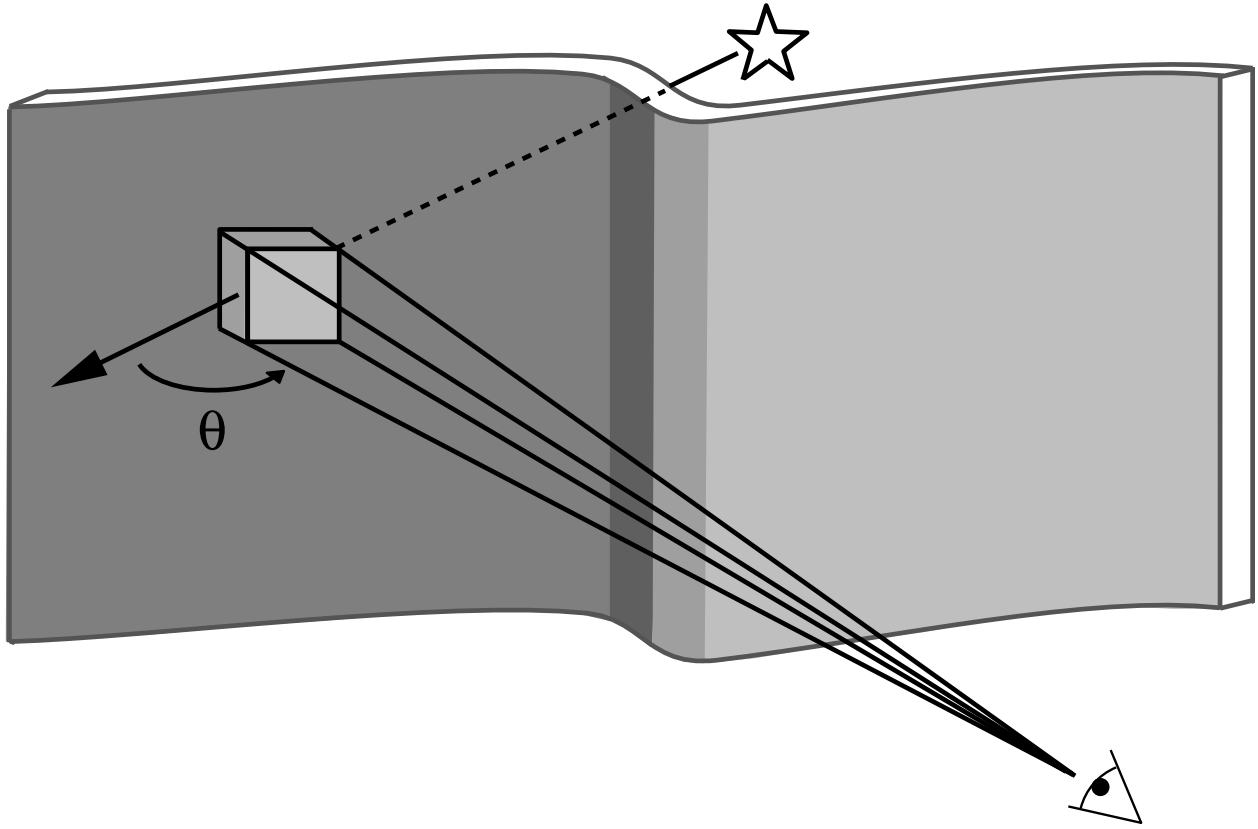
Fig. 2.— A simple reflection nebula interposed between the viewer and illuminating star. The box marks a *parcel* of nebulosity: the volume of dust corresponding to one pixel or resolution element as seen by the observer. Our model presumes the nebula is thin enough in the sightline dimension to characterize all scattering events within the parcel by the same deflection angle θ.
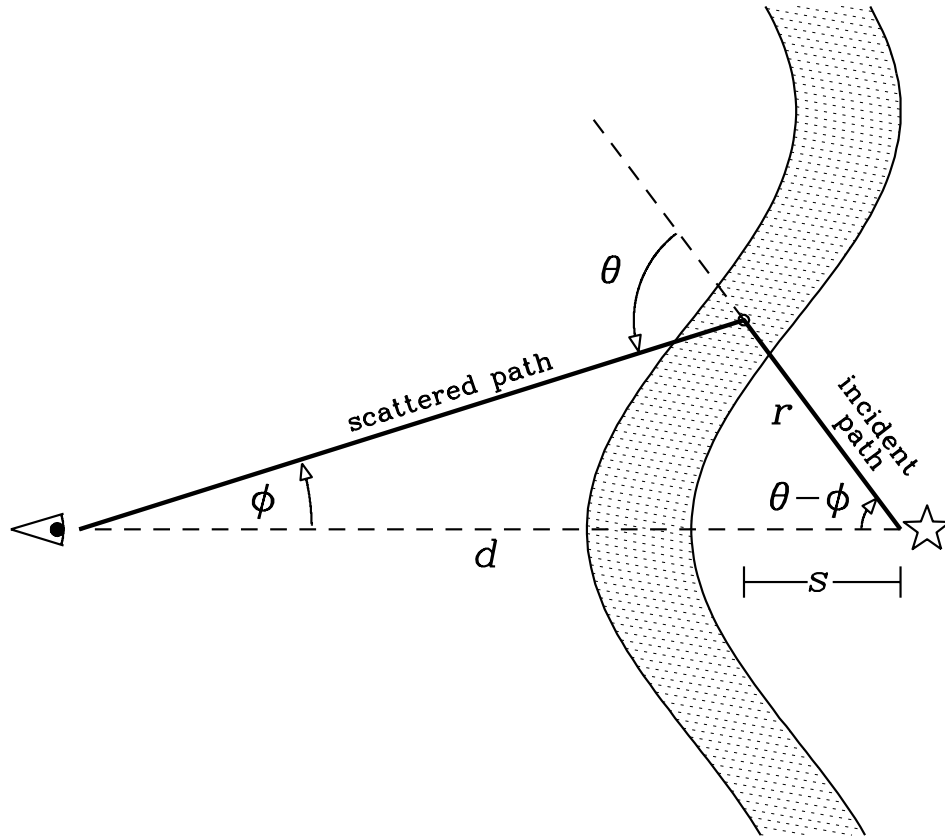
Fig. 3.— Scattering geometry in a generalized reflection nebula, showing the relationships between the observed star-parcel offset angle ϕ, grain scattering angle θ, star-observer distance d, star-parcel distance r, and star-nebula sightline separation $s = r \cos(\theta - \phi)$.
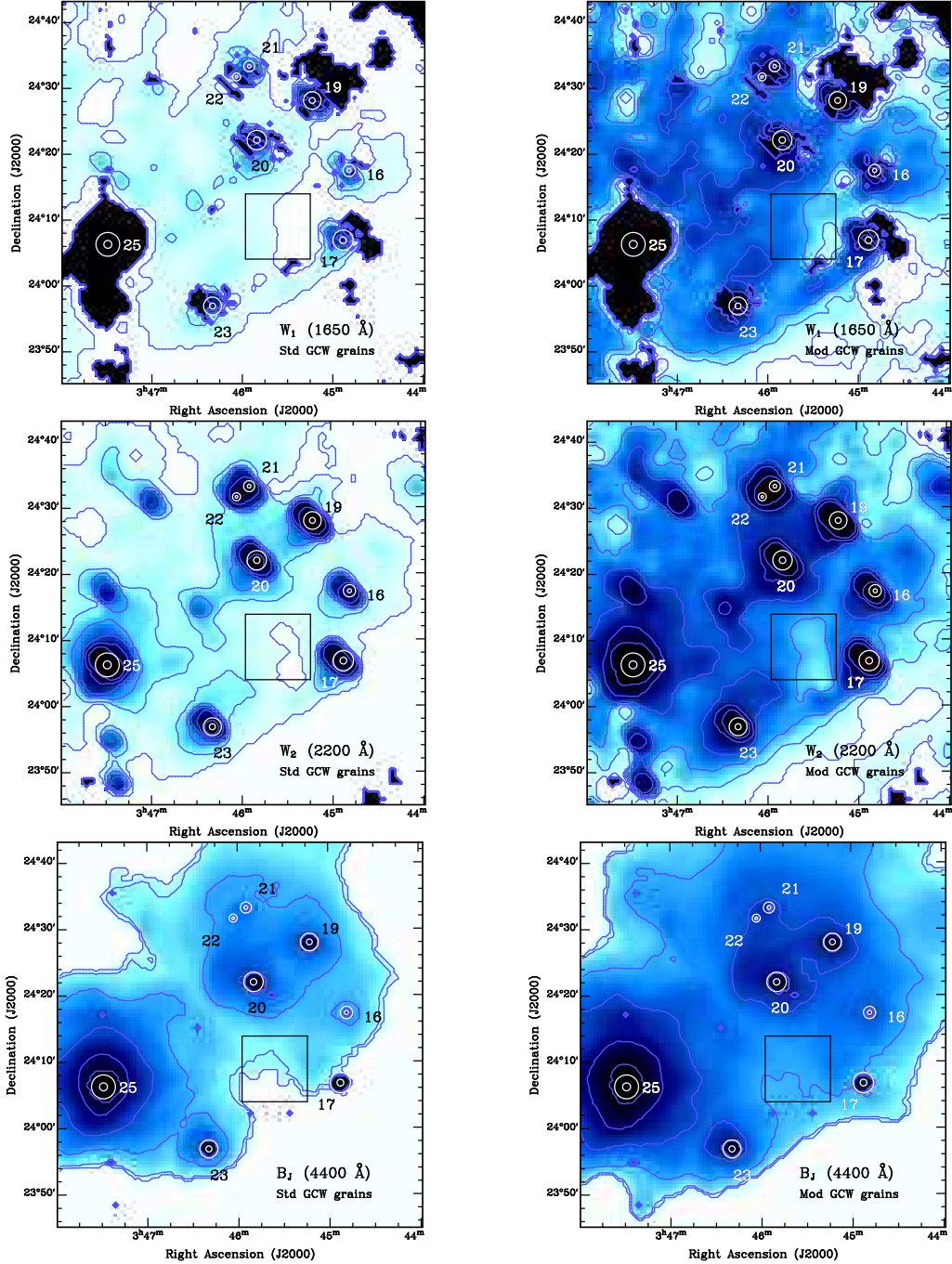
Fig. 4.— Scattering angle θ in the cluster core for two sets of scattering properties at three wavelengths. Intensities range linearly from $\theta = 15°$ (black) to $\theta = 90°$ (white), with contours marking 15° intervals. Backscattering angles are not shown. Stars have Flamsteed numbers. Left-side panels use standard GCW grains; right-side panels use UV-modified GCW grains. Both have a B7III input spectrum and smooth dust with $R_V = 3.1$ and $E_{B-V} = 0.05$ (Model A). Top, middle, and bottom panels show 1650 Å, 2200 Å, and 4400 Å, respectively. The box marks the main area used to measure differences between optical and UV angles (see §4.2).
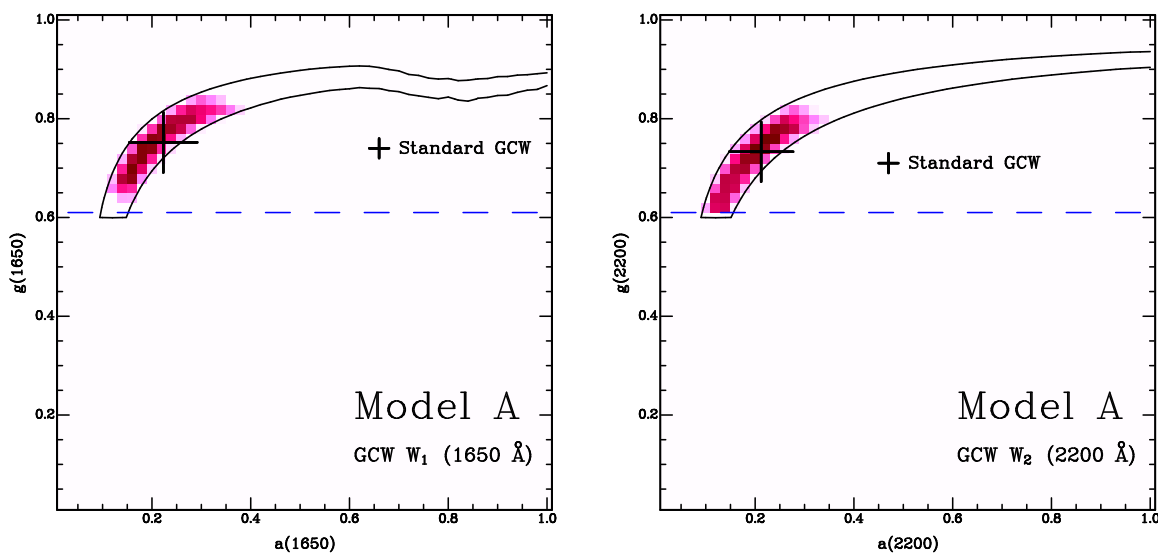
Fig. 5.— Illustration of the 4-D (a_1, g_1, a_2, g_2) solution space for the GCW Model A case. The panels show 2-D (a_1, g_1) and (a_2, g_2) slices through the average solution coordinates. UV-optical scattering angle absolute differences $|\Delta\theta|$ are indicated by shading over the range $0°$ (black) to $5°$ (white). The large crosses mark the average solutions, with the cross arms indicating 1σ standard deviations. The smaller crosses show standard GCW model (a, g) values. The horizontal dashed line marks $g(4400 \text{ Å}, \text{GCW})$. The contours show the extent of the same solution locus if the WBS photometry is not included in the analysis.
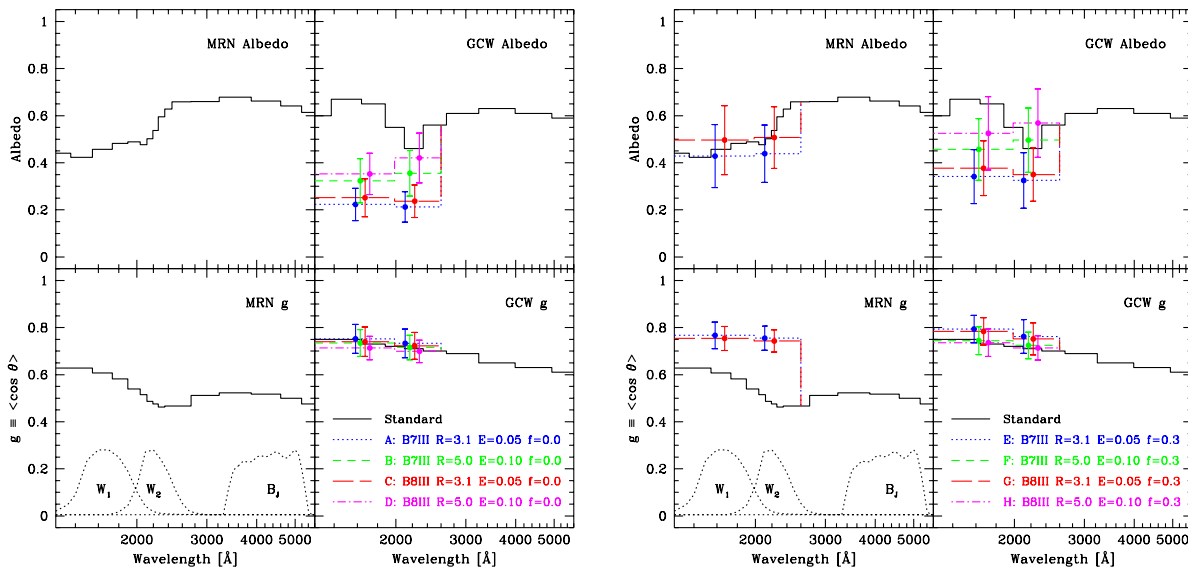
Fig. 6.— $a(\lambda)$ and $g(\lambda)$ solutions for the models listed in Tables 2 & 3. Only two MRN models had satisfactory (a, g) solutions. The solid lines connect standard MRN and GCW model values. The other line types connect revised (a, g) values for different cases. The horizontal bins indicate the wavelength ranges of the modified values. The dots marking the (a, g) solutions are staggered in λ for readability. Error bars give 1σ standard deviations. *WISP* 1650 and 2200 Å and Schmidt 4400 Å filter bandpasses are indicated.
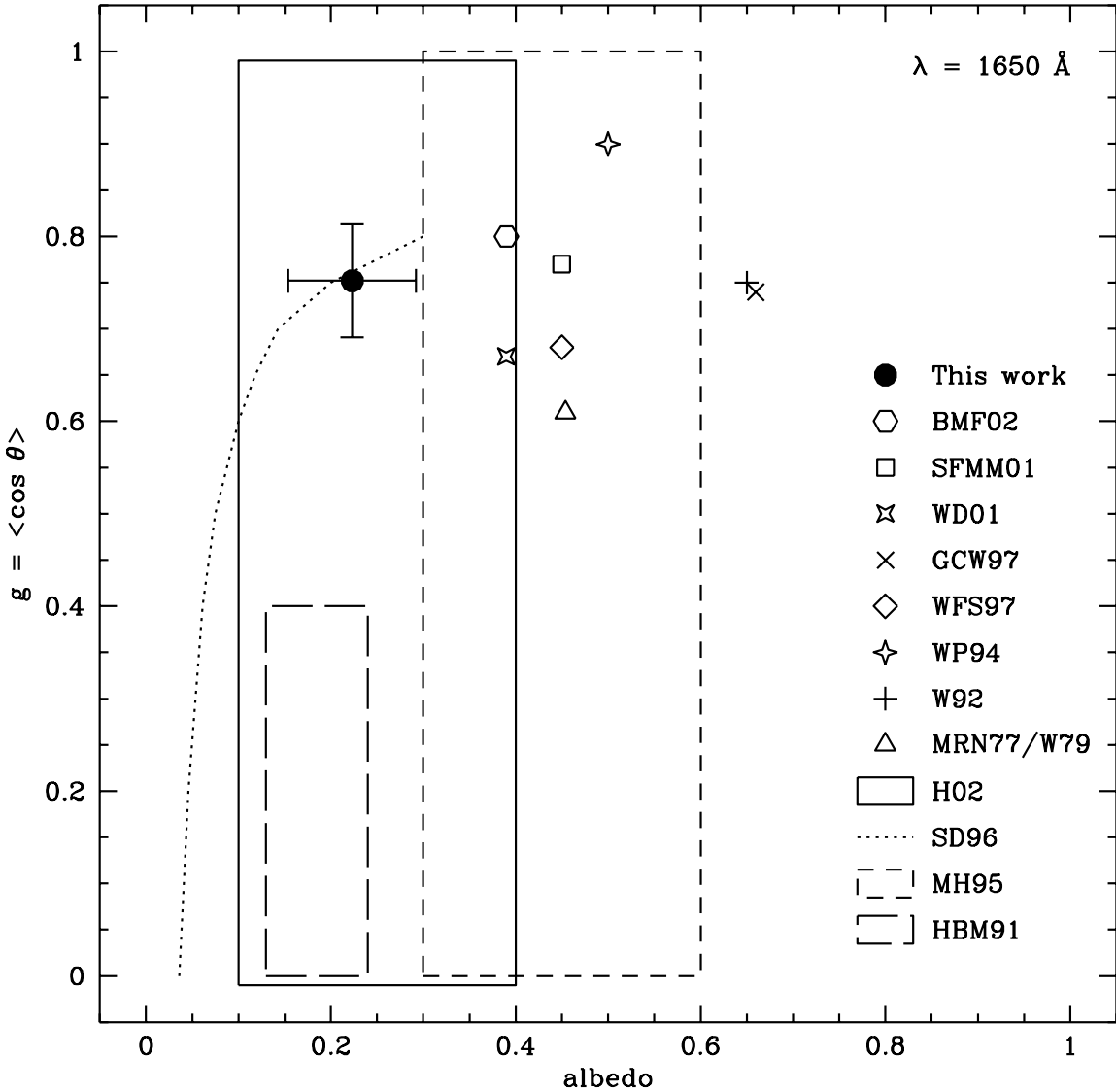
Fig. 7.— Our GCW Model A (a, g) values for the 1650 Å filter compared to other far-UV (a, g) results from Burgh et al. (2002), Henry (2002), Schiminovich et al. (2001), Weingartner & Draine (2001), Gordon et al. (1997), Witt, Friedmann, & Sasseen (1997), Sasseen & Deharveng (1996), Murthy & Henry (1995), Witt & Petersohn (1994), Witt et al. (1992), Hurwitz et al. (1991), and Mathis et al. (1977) via White (1979a). Typical 1σ errors quoted for the other results are $\sim 0.05 - 0.10$. The three boxes outline a or (a, g) ranges. The dotted curve shows (a, g) from Sasseen & Deharveng (1996). Though many have different wavelength ranges, all these studies include the WISP 1650 Å bandpass at least partly. The Burgh et al. (2002) values are from their longest-wavelength bin of $1345 - 1380$ Å. The Weingartner & Draine (2001) values are for $R_V = 3.1$.
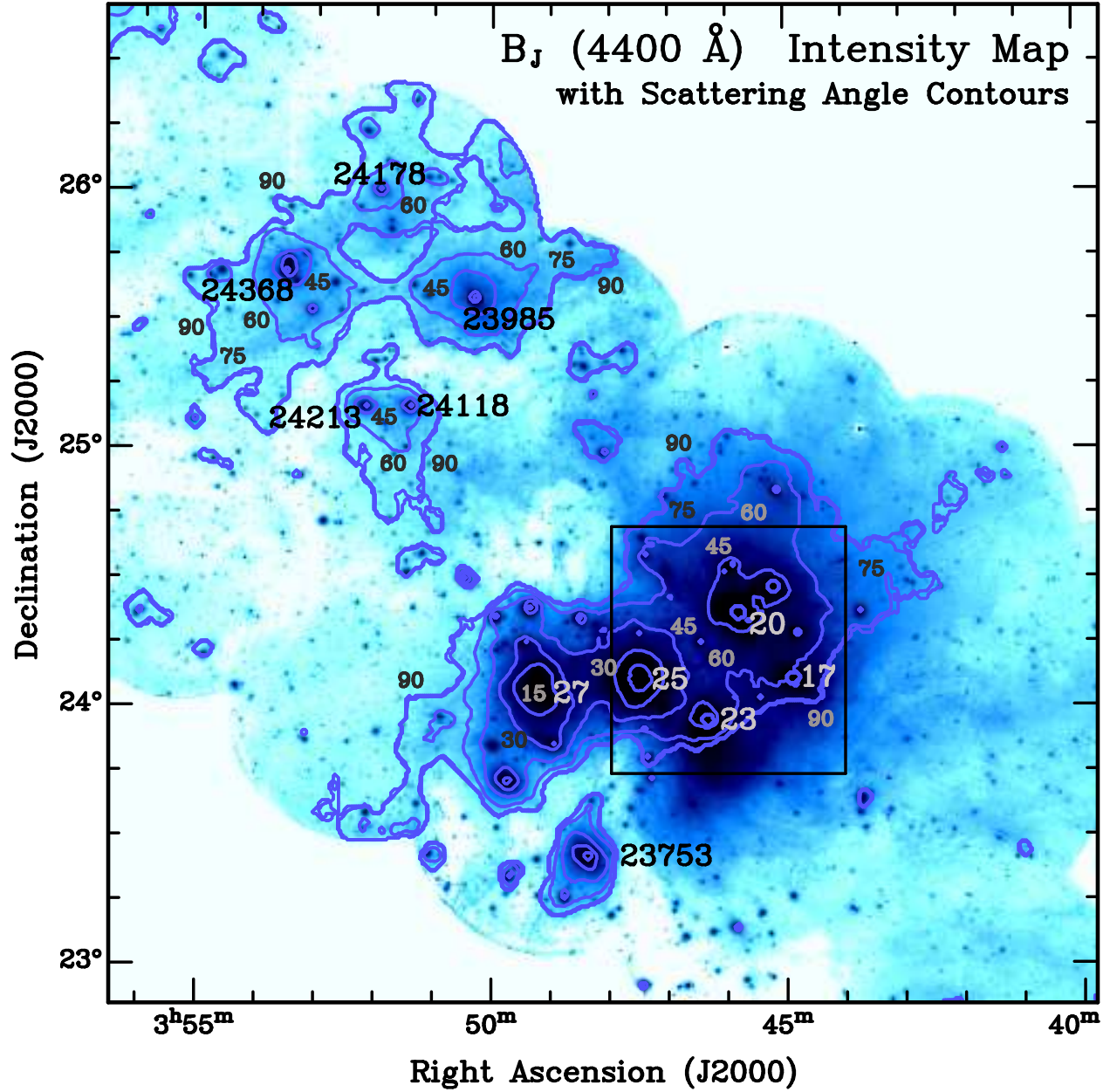
Fig. 8.— 4400 Å scattering angle contours for $\theta = 15°$, $30°$, $45°$, $60°$, $75°$, and $90°$ overlaid on Schmidt mosaic optical brightness from Paper I; the $75°$, and $90°$ contours are often close together. The intensity scale is that of Fig. 1. The angles are calculated for a UV-modified Model A nebula (Table 3). Small numbers label selected contour values in degrees. Stars discussed in the text are labeled with larger Flamsteed and Henry Draper numbers. The box marks the area of Fig. 4.

– 35 –

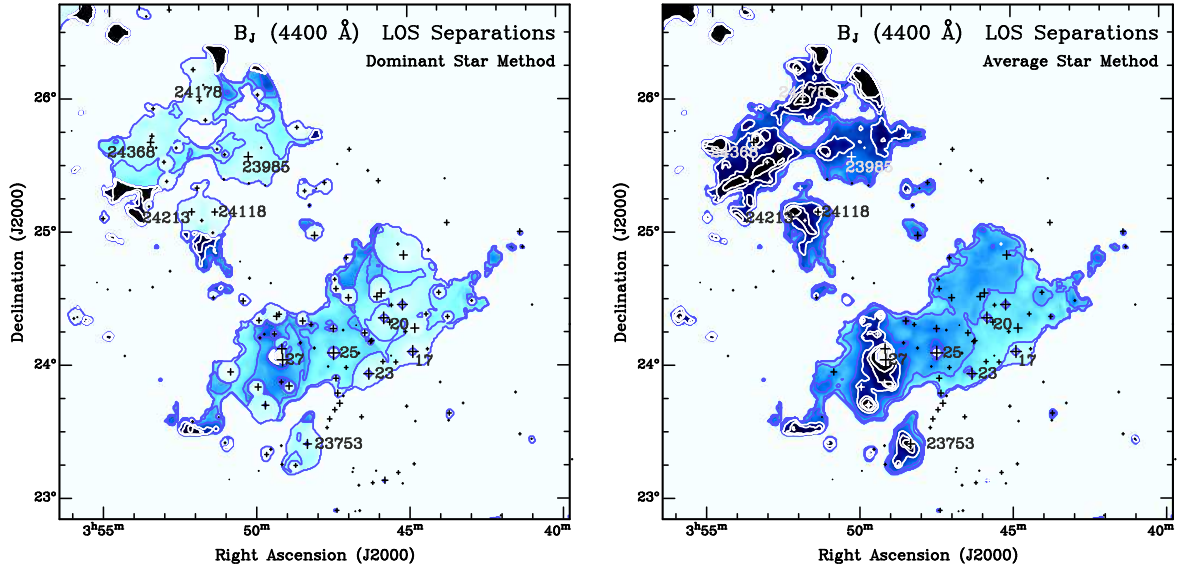Fig. 9.— 4400 Å star-nebula sightline separations for *(a)* dominant-star and *(b)* average-star offsets (§5.2.1). Intensities range from 0.00 pc (white) to 1.50 pc (black), with dark contours at 0.00, 0.25, 0.50, and 0.75 pc, and light contours at 1.00, 1.25, and 1.50 pc. All indicate foreground separations; background separations are not shown. Crosses mark bright stars. The area and star labels are as in Fig. 8.
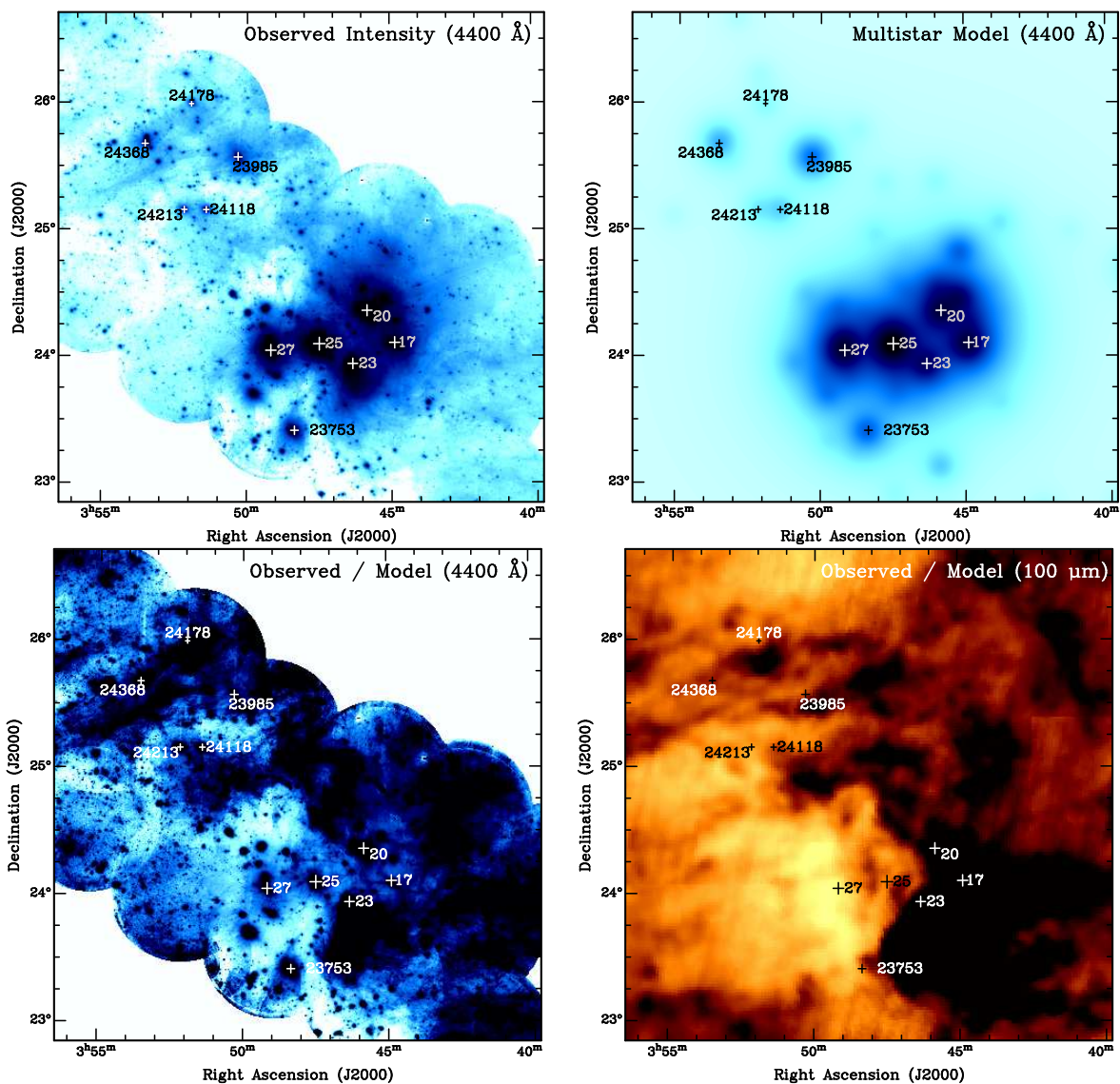
Fig. 10.— Multiple illuminator results for a UV-modified Model A nebula 0.7 pc in front of the stars. The two upper panels compare *(a)* 4400 Å intensity and *(b)* 4400 Å multistar model intensities on the same scale as Figs. 1 & 8. The two lower panels compare *(c)* observed 4400 Å intensity divided by the model and *(d)* the same for 100 μm. The ratios range linearly from 0 (white) to 2 (black). The area and star labels are as in Figs. 8 & 9.
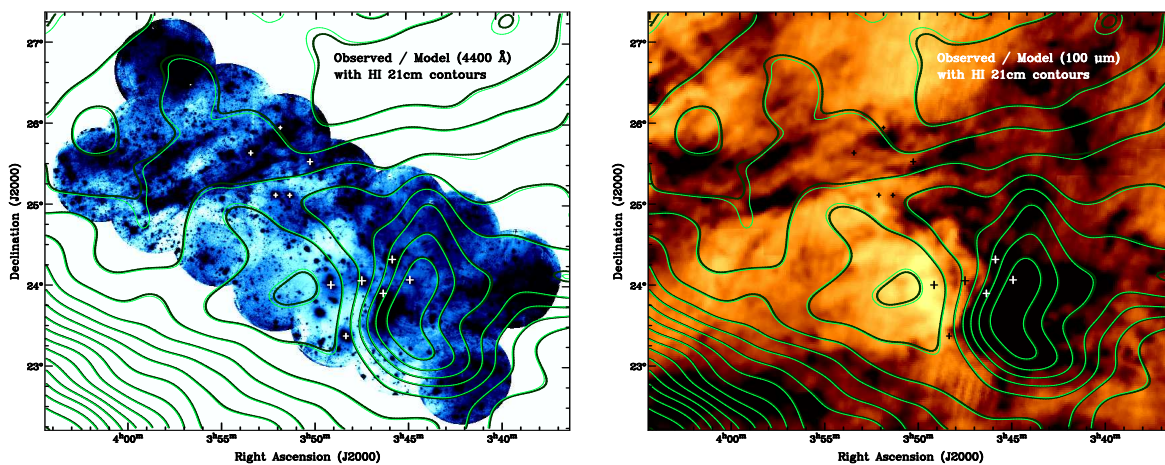
Fig. 11.— Observed/model intensity ratios as in Fig. 10 over a larger area, with H I 21cm emission contours from the Green Bank 43m telescope. The contours mark 2 K intervals in brightness temperature for gas at $+10.3$ km s^{-1} with respect to the Local Standard of Rest. The dark contours are 0.1 K below the light contours to indicate the local gradients. The maximum contour in the heavy nebulosity on the west side of the cluster core is 24 K. Crosses mark the stars labeled in Figs. 8-10.

Table 1.   Single-Star Model Parameter Space Grids

Search	Parameter	Values Used
primary grid: fixed (a, g) (§4.3.1)	$F_*(\lambda)$ E_{B-V} R_V[†] $f_c(\mathrm{UV})$ $a(\lambda), g(\lambda)$	B7III, B8III, B9III Kurucz spectra[*] 0.00, 0.03, 0.05, 0.10 3.1, 4.0, 5.0 0.00, 0.05, 0.10, 0.20, 0.30 MRN, GCW values (see Table 2)[‡]
secondary grid: variable (a, g) (§4.3.2)	(F_*, R_V, E_{B-V}, f_c) optical (a, g) $a(1650)$ $g(1650)$ $a(2200)$ $g(2200)$	selected combinations (see Table 3) MRN, GCW values $0.02, 0.04, 0.06, ..., 1.00$ $0.02, 0.04, 0.06, ..., 1.00$ $0.02, 0.04, 0.06, ..., 1.00$ $0.02, 0.04, 0.06, ..., 1.00$

[*]Kurucz (1993) atmosphere models with T_{eff} = 13000 K, T_{eff} = 12500 K, and T_{eff} = 11000 K, respectively, all using $\log g = 3.5$ and $\log (Z/Z_\odot) = 0$

[†]specifies a Cardelli et al. (1989) extinction curve

[‡]MRN = Mathis et al. (1977) and White (1979a); GCW = Gordon et al. (1997)

Table 2.   Standard Grain Model Properties

Grain Model	1650 Å		2200 Å		4400 Å	
	a	g	a	g	a	g
MRN	0.45	0.61	0.52	0.48	0.66	0.52
GCW	0.66	0.74	0.47	0.71	0.61	0.63

Table 3.   Revised UV Properties

	Nebular Model				Grain		1650 Å				2200 Å		
Name	$F_*(\lambda)$	R_V	E_{B-V}	$f_c(\mathrm{UV})$	Model	$a_1{}^*$	σ_{a_1}	g_1	σ_{g_1}	a_2	σ_{a_2}	g_2	σ_{g_2}
A	B7III	3.1	0.05	0.0	MRN†	—	—	—	—	—	—	—	—
					GCW	0.22	0.07	0.75	0.06	0.21	0.06	0.73	0.06
B	B7III	5.0	0.10	0.0	MRN	—	—	—	—	—	—	—	—
					GCW	0.32	0.09	0.73	0.06	0.36	0.10	0.72	0.05
C	B8III	3.1	0.05	0.0	MRN	—	—	—	—	—	—	—	—
					GCW	0.25	0.08	0.74	0.06	0.24	0.07	0.72	0.06
D	B8III	5.0	0.10	0.0	MRN	—	—	—	—	—	—	—	—
					GCW	0.35	0.09	0.71	0.05	0.42	0.11	0.70	0.05
E	B7III	3.1	0.05	0.3	MRN	0.43	0.13	0.77	0.06	0.44	0.12	0.75	0.05
					GCW	0.34	0.11	0.79	0.06	0.33	0.12	0.76	0.07
F	B7III	5.0	0.10	0.3	MRN	—	—	—	—	—	—	—	—
					GCW	0.46	0.13	0.74	0.06	0.50	0.14	0.72	0.06
G	B8III	3.1	0.05	0.3	MRN	0.50	0.15	0.75	0.05	0.51	0.13	0.74	0.05
					GCW	0.38	0.12	0.78	0.06	0.35	0.11	0.75	0.07
H	B8III	5.0	0.10	0.3	MRN	—	—	—	—	—	—	—	—
					GCW	0.53	0.16	0.74	0.06	0.57	0.15	0.71	0.05

*The 1650 Å albedo a_1 also applies to grain heating for $1000 \le \lambda \le 1350$ Å; see §4.2 for details.

†Most MRN models had no (a, g) solutions with $|\Delta\theta| \le 5.0°$; see §4.3.2.